PUBLICATIONS OF THE ASTRONOMICAL SOCIETY OF THE PACIFIC, **121**:498–511, 2009 May

UnISIS: Laser Guide Star and Natural Guide Star Adaptive Optics System

LAIRD A. THOMPSON,[1] SCOTT W. TEARE,[2] YAO-HENG XIONG,[3] RICHARD M. CASTLE,[1] ABHIJIT CHAKRABORTY,[1,4] ROBERT A. GRUENDL,[1] AND ROBERT W. LEACH[5]

Received 2008 June 24; accepted 2009 April 5; published 2009 May 20

ABSTRACT. UnISIS (University of Illinois Seeing Improvement System) is a versatile adaptive optics system mounted on a large optics bench at the coudé focus of the Mount Wilson 2.5-m telescope. It was designed to have both laser guide star (LGS) and natural guide star (NGS) adaptive optics capabilities. The LGS side of the system relies on a pulsed UV laser with raw power of 30 W capable of creating an artificial laser star via Rayleigh scattering 18 km above the telescope. The LGS system can work at temporal response rates as high as 333 Hz—limited by the UV laser pulse rate—and the NGS system can work at rates up to 1.4 kHz. Each side of the system has its own high-speed wavefront sensor that runs separately, but in the LGS mode the NGS wavefront sensor is converted into a natural star tip-tilt sensor. The deformable mirror is conjugate to the telescope's primary mirror and has one of the most densely packed sets of actuators of any adaptive optics system currently in operation. This paper provides details of the UnISIS design and describes key updates we have made to the system. We show NGS AO-corrected images from the sky from the 900 nm z-band through the 2.12 μm K_s band. The highest NGS Strehl achieved to date is 0.67 at K_s band.

Online material: color figure

1. INTRODUCTION

Many adaptive optics (AO) systems have been designed and built to produce diffraction-limited images at the focal plane of ground-based telescopes. AO systems were first conceived more than 50 years ago by Babcock (1953), and their early development (see Hardy 1998) was slowed by the lack of adequate technology like detectors, deformable mirrors, and fast computers. With AO components now readily available, it is not surprising that virtually all large astronomical telescopes have AO systems and that their number and diversity continues to grow at a rapid pace. Successful AO systems are now operating at the Keck Observatory (Wizinowich et al. 2006), the MMT Observatory (Milton et al. 2008), the VLT (Strobele et al. 2006), Palomar Observatory (Roberts 2008), the Gemini Observatories (for ALTAIR see Boccas et al. 2006; for the MCAO development see Rigaut et al. 2000; and for NICI see Toomey & Ftaclas 2003 and Chun et al. 2008), the Subaru Observatory (Takami et al. 2004), the Advanced Electro-Optical System (AEOS) telescope (Roberts & Neyman 2002), to name a few.

Natural guide star (NGS) AO systems were the first to be developed, and then, in the 1980s, experiments were started on laser guide star projection (Foy & Labeyrie 1985; Thompson & Gardner 1987; Happer et al. 1994). Laser guide star (LGS) AO systems rely on a laser beacon to illuminate a spot in the Earth's atmosphere. Backscattered light can be produced at altitudes between 10 and 30 km by Rayleigh scattering or at altitudes of 90 –95 km by resonant backscattering from atmospheric sodium atoms. LGS AO systems are among the most complex of astronomical instruments because of the need to operate these systems in a closed loop at high temporal bandwidths, the need to operate end to end at or close to the telescope's diffraction limit, and the need to incorporate high-power laser transmission in the system design. As the astronomy community carries AO system design into the realm of extremely large telescopes, it is important to document the experience gained from more modest AO systems, especially those that achieve Strehl ratios $>50\%$.

UnISIS was initially conceived and designed as a Rayleigh LGS AO system in the era when the U.S. Air Force was declassifying their pioneering work on laser-guided AO (Fugate et al. 1994). This happened after Foy & Labeyrie (1985) suggested in the open literature that lasers and AO systems would make a good match. Concurrent with the initial tests on the sky of both sodium (Thompson & Gardner 1987) and Rayleigh (Thompson et al. 1991; Thompson & Castle 1992) LGSs, Thompson and Gardner submitted proposals to the U.S. National Science

[1] Astronomy Department, University of Illinois Urbana-Champaign, Urbana, IL 61801; thompson@astro.uiuc.edu, gruendl@astro.uiuc.edu.

[2] Electrical Engineering Department, New Mexico Tech, Socorro, NM 87801; teare@ee.nmt.edu.

[3] Yunnan Observatory, Chinese Academy of Sciences, P.O. Box 110, Kunming, China 650011; xyh@ynao.ac.cn.

[4] Physical Research Laboratory, Ahmedabad 380009, India; abhijit@prl.res.in.

[5] Astronomy Department, San Diego State University, San Diego, CA 92182; leach@astro-cam.com.

Foundation with the aim of building the first LGS AO system (Thompson & Gardner 1989; Gardner et al. 1990 and references therein). Although the first two NSF proposals (by Gardner and Thompson in 1987 and 1988) were rejected, NSF support for laser-guided AO work accelerated after May 1991, when the U.S. Air Force research group at Starfire Optical Range (SOR) announced that it had succeeded in a top secret research program to operate the first LGS AO system (as later reported by Fugate et al. (1994).

UnISIS shares design characteristics with the original SOR LGS system, not the least of which is the choice of Rayleigh scattering as a means of creating the LGS. While all early groups recognized the advantages of using sodium LGSs, sodium lasers that are sufficiently powerful to be used in an AO system were not available in the early 1990s, and today they are still costly to obtain and operate. The Rayleigh LGS system at SOR used a copper vapor laser working in green wavelengths around 530 nm, whereas UnISIS uses an Excimer laser that works in the near-UV at 351 nm (Thompson & Teare 2002; Paper I). A third Rayleigh LGS system is nearing completion at the Isaac Newton Group (ING) of telescopes on La Palma, Spain. The ING team is installing a frequency doubled Yb:YAG laser that emits at 515 nm on the William Herschel 4.2-m telescope. This new Rayleigh LGS system will be used with the existing NAOMI adaptive optics system (Rutten & Talbot 2005) for ground-layer adaptive optics (GLAO) work. Plans have also been made at the SOAR Telescope to build yet another GLAO system based on a Rayleigh laser beacon (Tokovinin 2004), and the MMT has a multiple Rayleigh laser guide star system that recently came into operation (Baranec et al. 2009).

UnISIS is now operational, and this paper aims to summarize technical details of the system, many of which are of importance to our own future science observations as well as to others who are designing or building AO systems for moderate aperture telescopes. We discuss the UnISIS optical configuration, describe its two science cameras, its new RealTime Linux AO closed-loop control system that is capable of running at update rates that exceed 1 KHz, our new Pockel's cell switch to time-gate the LGS return signal, the UnISIS four-prism atmospheric dispersion compensator, as well as other topics. We present closed-loop NGS performance data from the sky and interpret these performance data in terms of predicted wavefront errors. The status of UnISIS was last discussed by Thompson et al. (2004) where we described on-the-bench tests of the closed-loop LGS system and the methods we use to calibrate the LGS wavefront sensor. In the current paper we present previously unpublished NGS results, emphasize changes we have made since we last reported on the status of UnISIS, and discuss the impact these changes have made in terms of system performance.

2. UNISIS OPTICAL CONFIGURATION

The coudé optical train of the Mount Wilson 2.5-m telescope is a three-mirror system—primary, secondary, tertiary—that transfers a converging f/30 beam down the telescope's south polar axis to the fixed coudé focus (see Figure 1 in Thompson & Teare 2002). The primary mirror was polished by George Ritchey in the early 1900s to a superb figure (Ritchey 1928) with peak-to-valley surface irregularities of $\sim$75 nm so that in reflection at 850 nm, the primary mirror delivers an rms wavefront $\sim\lambda/30$. While no optical test information exists for the f/30 secondary mirror, George Ritchey polished it, too. We installed a newly polished large tertiary mirror in 2004, and it also has an exquisite surface. These points are significant because optical surface irregularities with scales smaller than the 20 cm separation of the UnISIS deformable mirror actuators will degrade the AO performance. We note that another group took advantage of the excellent 2.5-m telescope optical system and built a NGS AO system for the telescope's bent Cassegrain focus (Shelton et al. 1997).

During its entire history of operation, the Mount Wilson 2.5-m telescope has delivered excellent images well into the subarcsecond regime (Teare et al. 2000; Teare & Thompson 2002), but excellent performance comes only when the soda-lime "plate" glass primary mirror is in thermal equilibrium with the surrounding air. Our experience shows that a temperature difference—between the back surface of the primary mirror and the surrounding air—larger than 1.8°C at any time in the previous 24 hr period compromises the telescope's optical performance by warping the primary mirror (cf., Ritchey 1928). Temperatures on and around the primary mirror are monitored when UnISIS is scheduled for operations, and we proceed with caution if δT is measured to be larger than the 1.8° limit. The UnISIS deformable mirror can remove temperature-induced "static" primary mirror deformations even when the air-to-glass temperature differences are as high as 2.5°C. However, when the UnISIS LGS is sent into the sky by reflecting it off the telescope primary mirror, no adaptive correction is applied to the transmitted laser beam. As a result, UnISIS LGS operation is limited to those times when the primary mirror has been within the 1.8°C limit of the surrounding air for $\sim$24 hr.

Early in the UnISIS project we found that the tertiary mirror that was used with the 2.5-m telescope for the first 80 years—a circular mirror 20 inches in diameter—vignetted the telescope pupil for all target stars north of 29° declination, and the extent of the vignetting increased with declination. The basic issues and the solution to this problem were discussed in Thompson et al. (2003a). We report here the optical quality of the newly polished 20×40 inch tertiary mirror that replaced the older smaller tertiary. The Precision Optics Division of Eastman Kodak Company polished the large tertiary mirror to an exquisitely flat figure with the small tool method (repeated polishing sessions followed by precision surface metrology). Four such iterations yielded a surface flatness better than 1/10 wave rms at 633 nm exclusive of the outer perimeter (17 mm wide), which has a turned down edge, well outside the optical clear aperture of the telescope.

All UnISIS AO components are mounted on a large optics bench, the front edge of which protrudes into the coudé room just above the Coudé spectrograph slit mechanism where the original f/30 coudé beam came to a focus. A smaller auxiliary optics bench is kinematically mounted on the front end of the main bench to allow UnISIS mirrors M1, M2 (and other necessary components) to be placed just inside the f/30 coudé focus. These first two mirrors lift the f/30 coudé beam to a convenient height above the UnISIS optics bench even before the incoming telescope beam reaches its initial f/30 focus. There are times when the massive optics table is slightly out of thermal equilibrium with the air inside the telescope dome, but we see absolutely no evidence of degraded performance in these circumstances: the wavefront sensors show perfectly calm steady subimages and the on-the-bench Strehl performance is virtually perfect. This is because the optics table was designed to have a relatively tight insulated cover with one small open hole to admit the coudé beam. This cover restricts the flow of air within the optical system.

3. UnISIS OPTICAL DESIGN

As mentioned above, UnISIS mirrors M1 and M2 transfer the f/30 coudé beam and lift it onto the UnISIS optics table. Hand-actuated tip-tilt controls on M1 and M2 provide the 4 degrees of freedom needed to steer the main f/30 telescope beam into the UnISIS AO optical system, these 4 degrees of freedom being the x, y position of the pupil center and the two direction cosines of the telescope's optical axis.

The main UnISIS optical configuration was specified in close collaboration with optical designer E. Harvey Richardson. All optical elements are positioned in such a way that ample room exists to add additional components along the beam for a wide range of experimental purposes. The design is very simple. An f/30 off-axis parabola accepts the input beam from the telescope and produces an 89 mm diameter collimated beam. A second off-axis parabola that works at f/77 focuses this beam to a final image scale $\sim$1 arcsec mm^{-1}. The optical system reimages the 2.5-m primary mirror onto the deformable mirror. UnISIS has two Shack-Hartmann wavefront sensors, one to analyze the laser guide star signal and a second to analyze the natural guide star signal. This dual wavefront sensor (WFS) concept was first used by Fugate et al. (1994) and provides the ideal means of calibrating a LGS WFS on the sky in real time. The maximum unvignetted field of view of the entire UnISIS optical system is 1.3′ in diameter, but the science cameras used at the present time cover only a small fraction of this field.

Figure 1 shows a schematic drawing of the main optics table with the auxiliary optics table attached on the right where the optical system protrudes into the telescope's coudé room. The f/30 coudé beam enters the diagram from the right as it descends down the telescope's south polar axis. M1 reflects the beam upward toward M2, and then M2 diverts the beam to the left in the

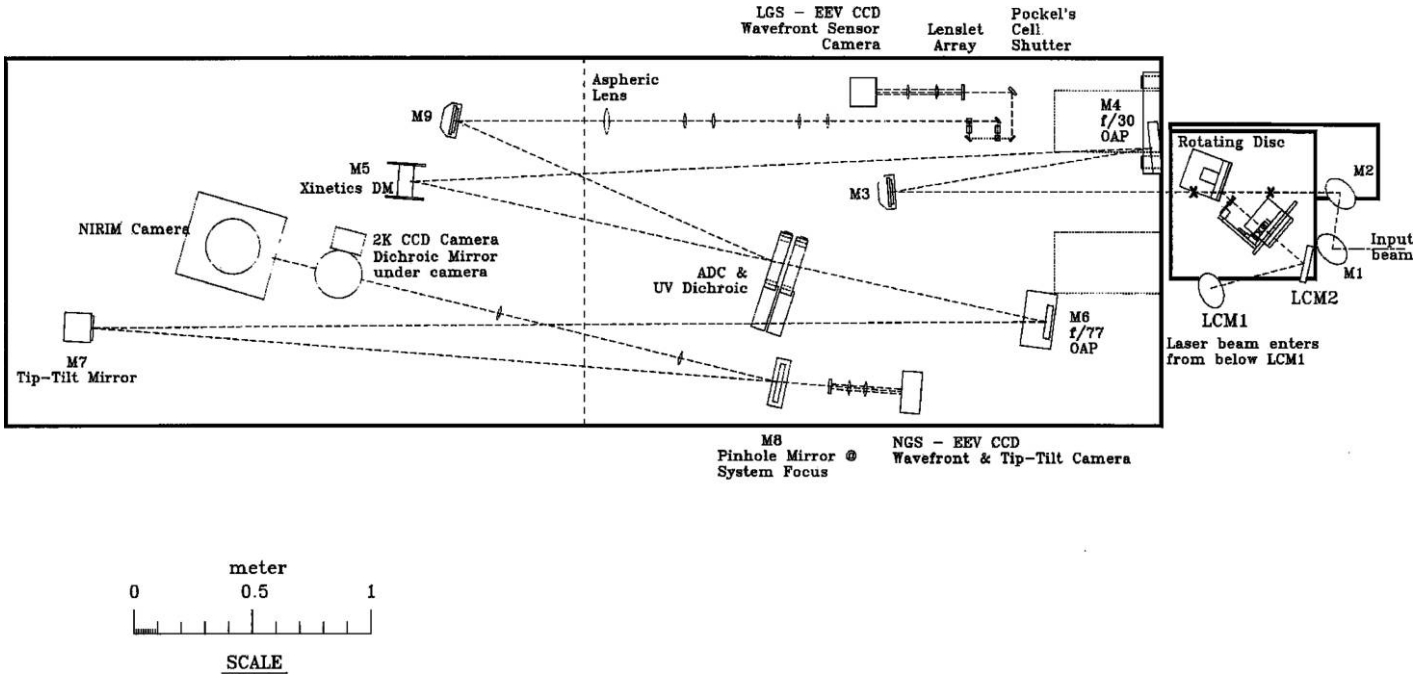

FIG. 1.—Component layout for the UnISIS optical system. Light enters on the right from the descending coudé beam. The large optics table is 5×16 feet. The smaller optics table on the right is kinematically suspended on the end of the large optics table and sits immediately above the old coudé spectrograph slit mechanism. As the incoming beam crosses the smaller optics table, two small X's can be seen along the dashed beam line, the first for the infinity focus and the second for the 18 km laser focus. Using the label "Rotating Disc" as a point of reference, these two X's sit below the letters "*o*" and "*s*".

diagram after it has risen to a height of 177 mm above the top surface of the main optics table. The optical axes of all remaining components in Figure 1 are also 177 mm above the optics table. In Figure 1 two X's can be seen along the f/30 input beam immediately after M2. The X on the right marks the location of the f/30 infinity focus, and the X on the left marks the conjugate point of the LGS's 20 km focus ~328 mm beyond the infinity focus. Between these two X's is a rotating glass disk that acts as a beam-sharing optical element allowing both incoming star light and outgoing laser light to use the main telescope optics. A schematic view of the component layout in this area can be found in Figure 2 of Paper I, where the beam-sharing scheme is described in detail.

Two components of UnISIS are not shown in Figure 1. The first of these is a removable 45° mirror that can be inserted into the main beam just beyond the LGS 20 km focus. Once this mirror is in the beam, incoming laser guide star light from the sky is directed to a simple lens. This lens forms an image of the laser guide star on the detector of a commercial ITT camera (type F-4576) that consists of a time-gated image intensifier and its Reticon silicon array. The intensified Reticon camera records images of the focused LGS return signal. It is used only for LGS testing. A second feature not shown in Figure 1 is the field acquisition camera for science operation. A remotely controlled flip-mirror can be raised in the light path between M1 and M2 thereby diverting star light into a wide-field video-rate CCD camera.

M3 is a plane mirror that folds the beam and sends it into M4, a collimating f/30 off-axis parabola (OAP). The OAP sends the beam to the Xinetics deformable mirror (M5) where the telescope primary mirror is reimaged onto the face of the deformable mirror (DM) with a pupil diameter of 89 mm. After reaching M5 the beam is directed toward the atmospheric dispersion corrector (ADC) system. Up to this point both star light and the returning LGS light travel along the same path. The two beams are separated at the front surface of the ADC, which is coated with a 99.9% reflective narrow band coating selected to deflect the UV laser guide star light toward M9. Note that the DM modulates the wavefronts of both natural star light and the returning LGS light. The LGS wavefront is immune to tip-tilt jitter and remains bore sighted with the telescope optical axis while natural star light suffers tip-tilt jitter that is removed further down the optical path.

The ADC rotates under servo-control as the telescope is pointed to various positions around the sky. After a failed effort to absolutely and precisely align the front optical surface of the ADC—to eliminate run-out or "wobble" in the reflected LGS beam—the ADC was mounted on a tip-tilt base plate that can be adjusted in real time to eliminate this minor annoyance.

Collimated star light passes through the ADC to the f/77 off-axis parabola. This mirror focuses the beam at a scale of 1.07 arcsec mm^{-1} at the detector, but before reaching focus the beam encounters tip-tilt mirror M7, which folds the beam back toward the AO focus at M8. In Figure 1, M8 is designated as the "pinhole mirror" even though this mirror can be easily swapped between a dichroic, an achromatic partially reflecting mirror, or the pinhole mirror itself. M8 sits at the AO system focal plane, and if an empty pinhole is placed at this focus, the pinhole functions in the same manner as a focal plane coronagraph in the sense that star light passing through the pinhole will not be reflected to the science camera focal plane. The sole requirement for M8—whether a pinhole, a partially reflecting mirror, or a dichroic is used—is that some light be allowed to pass through M8 into the NGS wavefront sensor (an E2V CCD). As explained in detail in § 8, the NGS E2V CCD camera (80×80 frame transfer CCD39-01) serves the dual functions of either (1) providing the error signal for the tip-tilt mirror M7 or (2) providing a wavefront image for the NGS Shack-Hartmann sensor. The pinhole mirror itself consists of aluminum deposited on glass, so it has the attractive characteristic of decreasing (but not totally eliminating) the light reflected at the surface of the glass substrate inside the outline of the pinhole. Three pinholes are available: 2.11″, 0.51″, and 0.21″ in diameter. When light from an AO-corrected bright star is focused on the center of the pinhole, this light is split in such a way that ~1% is reflected off the bare glass surface—thereby attenuating the bright star at the focal plane—while the remaining ~99% goes either to the tip-tilt sensor (in LGS operation) or to the wavefront sensor (in NGS operation).

Science light reflected off M8 is reimaged by two achromatic lenses that convert the image scale from 1.07 arcsec mm^{-1} (f/77) to 1.00 arcsec mm^{-1} (f/81.6). In most circumstances, two science cameras sit at the final UnISIS focal plane. These science cameras can be run separately or simultaneously. The most commonly used camera is called NIRIM. It contains a 256×256 NICMOS-3 array. Full details of this camera—including its carefully specified diffraction-limited cooled internal reimaging optics that match it to the UnISIS input beam—are described by Meixner et al. (1999). The second UnISIS science camera is a 2048×2048 red-optimized Loral CCD. Details of both cameras are given in Table 1. When the two science cameras are run simultaneously, the AO-corrected beam is split by a dichroic with a wavelength cut at 1.05 μm. It is a simple matter to replace this dichroic as the science needs change, or the dichroic can be removed from the beam so that all the light goes to NIRIM.

The end-to-end system throughput is given in Table 2 for four wavelengths that span the range over which UnISIS is sensitive. The sky backgrounds we observe through UnISIS are not significantly higher in the 750 nm to 1.65 μm range than those at excellent dark-sky observatories despite the visually bright night-sky contamination at Mount Wilson at shorter wavelengths. The background at wavelengths longer than ~1.8 μm depends on the thermal emission of both the telescope and the UnISIS optics. We find a background of ~11.5 mag arcsec^{-2} in the K_s band. NIRIM does not have a cold pupil mask to hide the

TABLE 1
UnISIS Science Cameras

NIRIM Array Camera	
Sensor:	256×256 HgCdTe NICMOS-3 array
Pixel size:	40 μm
Pixel scales:	0.04″ or or 0.08″ on a side (internal optics change)
Field of view:	$10'' \times 10''$ or $20'' \times 20''$
Spectral Coverage:	0.76–2.5 μm
QE:	75% (1.25 μm), 84% (1.65 μm), 89% (2.12 μm), 79% (2.25 μm)
RMS read noise:	40 e^-
Dark current:	50 e^- s^{-1}
Standard filters:	J (1.25 μm), H (1.65 μm), K_s (2.12 μm), K (2.25 μm)
2K CCD Camera	
Sensor:	2048×2048 Loral-Lick3 thinned backside-illuminate CCD
Pixel size:	15 μm
Pixel scales:	0.015 arcsec pixel^{-1} or 0.030 arcsec pixel^{-1} (2×2 binned)
Field of view:	limited by vignetting of optics and not by the sensor
Spectral Coverage:	300 nm–1.1 μm (60 nm HfO_2 coated for high red response)
QE:	98% (625 nm), 89% (750 nm), 52% (900 nm)
RMS read noise:	8 e^-
Dark current:	10 e^- per hour
Standard filters:	SDSS r' (625 nm), SDSS i' (750 nm), SDSS z' (900 nm)

secondary mirror support structure of the telescope, and this is the main contributor to the background at longer wavelengths. Even so, when we process multiple images and do a median sky subtraction, we can detect stellar (point) sources as faint as $K_s \sim 16$ (3 σ detection) in a total exposure time of 60 s.

A conjugate image of the telescope's primary mirror is located midway between the two achromats. This is a convenient location to insert coronagraphic pupil masks. Chakraborty et al. (2005) placed a Gaussian-shaped pupil mask here to conduct lab-bench coronagraphic imaging tests. Because the UnISIS optics table is easy to access, a wide variety of coronographic configurations can be easily swapped in and out. For example, we have tested the system with a uniformly coated partially reflecting surface at M9, an annular pupil mask at the pupil image between the two achromats, and a totally reflective 0.5″ diameter focal plane obscuration inside NIRIM at the final focal plane of the two achromats.

One very necessary subsystem not shown in Figure 1 is a high-speed video camera that is used to monitor the AO correction in real time. A small flip-mirror can be inserted in the beam between the last achromat and the science cameras to divert the final AO-corrected focal plane to the high-speed video camera. Just before AO-corrected images are captured with either or both of the science cameras, this high-speed video camera is used to monitor AO performance. Once the high-speed video camera shows that the AO system has been optimized after varying the AO feed back gain and damping, the flip-mirror is removed, and science images are captured.

4. NEW LGS WFS POCKELS CELL SWITCH

As described in Thompson et al. (2002), the LGS WFS relies on a Pockel's cell switch to time-gate the returning LGS signal. Because the Pockel's cell works only on polarized light, the optics must divide the incoming collimated LGS beam into two polarizations, and once the switching is completed, these two beams must be recombined before the LGS light goes to the Hartmann lenslet array. In the first design (Thompson et al. 2002), the beam was split with two polarizing calcite Thompson prisms. However, the long path length through the calcite (32 mm to divide the beams and another 32 mm to recombine them) caused significant 351 nm absorption. With ~0.84

TABLE 2
System Throughput

	I band (750 nm)	z-band (900 nm)	H band (1.65 μm)	K_s band (2.12 μm)
Telescope (3 reflections)	0.59	0.70	0.80	0.80
Transfer to Optics Table	0.67	0.73	0.79	0.78
Reimaging Optics and ADC	0.29	0.39	0.49	0.36
Camera QE	0.89	0.52	0.84	0.89
Total	0.10	0.10	0.26	0.20

transmission per prism, two prisms in series transmitted only ~71% of the entering photons. In order to maintain high throughput, the calcite prisms were replaced with fused silica cube beam splitters from CVI Laser, Inc. (Albuquerque, NM). The old design had a "bow-tie" layout, and the new design (briefly described in Thompson et al. 2003b) has a simpler square configuration that is shown in Figure 2. The CVI cube beam splitters have 99% throughput at 351 nm, and fortuitously they leak at the 635 nm wavelength of the alignment laser. This provides a significant advantage when doing the optical alignment because the 635 nm beams propagating through the new Pockel's cell switch create fringes that are easy to see in two secondary beams that escape the cube beam splitters. The new CVI Pockel's cell switch works best at 351 nm when the angular direction and the overlapping positions of the two escaping 635 nm beams cancel at null fringes.

5. DEFORMABLE MIRROR AND CONTROL MATRICES

The UnISIS DM and its HV drive electronics rack were purchased from Xinetics Inc. (Devon, MA). 177 PMN (lead magnesium niobate) actuators provide the thin glass face-sheet an unconstrained mechanical stroke at the DM surface of 4 μm. After limiting actuator throws to the linear range, the mirror surface is free to move ~3 μm thus producing a total optical stroke of 6 μm in reflection. This is more than is required to control the wavefront in good seeing conditions, and the extra stroke is useful in NGS operation when the primary mirror is somewhat out of thermal equilibrium. DM actuators have the standard Xinetics 7 mm spacing in both vertical and horizontal directions. The 2.5-m telescope primary mirror is imaged onto the front surface of the DM in such a way that 12.7 actuators span the full pupil of ~89 mm giving a 20 cm actuator-to-actuator separation at the primary mirror.

The geometric relationship between the DM actuators and the wavefront sensor gradients defines the mathematics of the AO closed-loop operation. A control matrix provides the link between the measured WFS gradients and the output commands to the DM actuators. We use a standard "Fried" geometry with actuators at the corners of Hartmann subimages. An array of 12×12 gradients serves the 13×13 array of actuators. Figure 3 shows the layout at the telescope pupil.

Of the 177 DM actuators, 9 fall inside the telescope's central obscuration, 40 fall entirely outside the pupil, and the remaining 128 are active in the clear portion of the telescope pupil. With 128 actuators in a 2.5-m diameter pupil, UnISIS has one of the highest actuator densities among all astronomical AO systems. We slave the 5 innermost as well as 32 perimeter actuators by

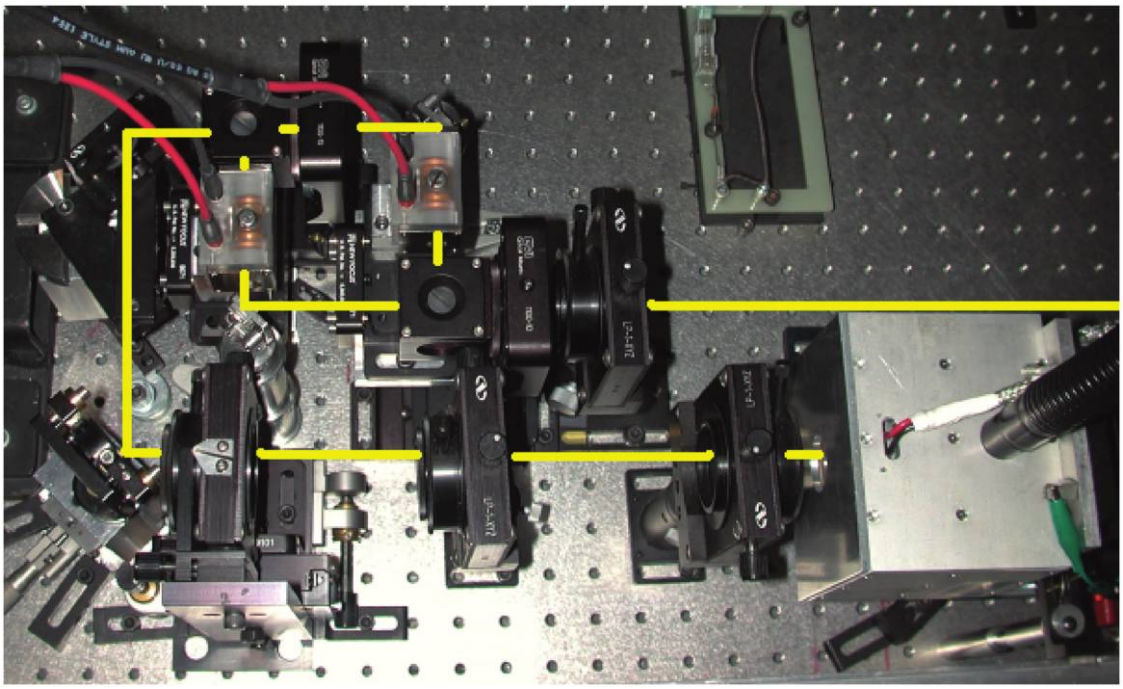

FIG. 2.—CVI Pockel's cell switch. The LGS E2V WFS camera head is housed in the cubical aluminum box at the lower right. LGS light enters the picture from the right side along the heavy horizontal line as it passes along the far edge of the E2V camera head. The optical switch is a square configuration at the upper left. The two Pockel's cells—one for each polarization—can be identified by their HV wires (one red and one black). The recombined output from the optical switch is redirected in a CCW direction by two mirrors, and the optical path into the EEV camera head runs from left to right. The Hartmann lenslet array and two camera lenses can be seen along the bottom of the picture where the light is passing from left to right into the camera head. The same beam path can be traced in the schematic layout in Fig. 1, but note that the schematic must be rotated 180° to correspond 1:1 to the photograph shown here.

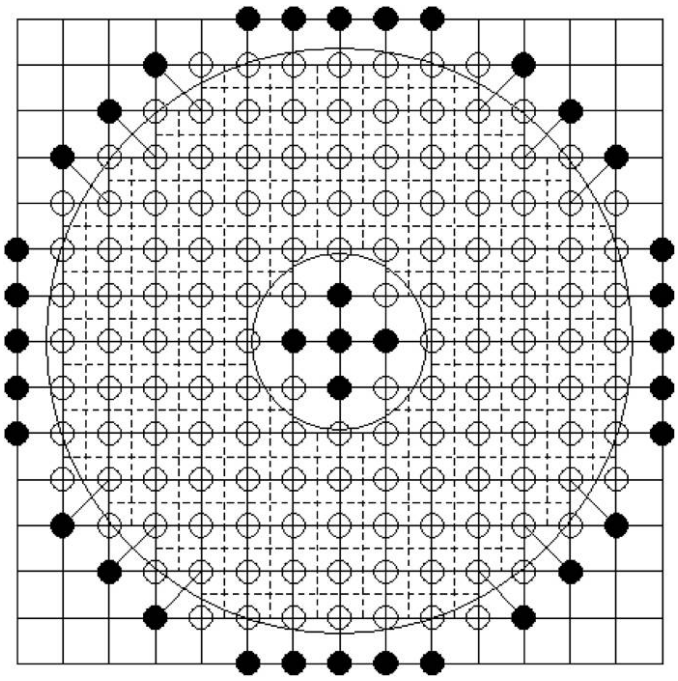

FIG. 3.—Deformable mirror actuator map. The annular telescope pupil is shown here projected onto the deformable mirror. The 177 small circles represent individual DM actuators. Note that actuators sit at the corners of WFS quadcells; quadcells are defined by the solid horizontal and vertical lines. Filled circles represent "slaved" actuators that are coupled to their closest active radial neighbor (connected with solid lines).

giving them signals from their closest radial neighbor (inner neighbor for the outer actuators and vice versa for the inner actuators). There are 140 actuators either in the pupil or just outside the pupil at the corners of active gradients. Whether a gradient is used or not in closed-loop operation depends on whether its subimage falls on an illuminated portion of the pupil. There are four partially illuminated gradients located closely adjacent to the central obscuration (but not inside that area), and we have run experiments to check the system performance with and without them. We see little to no difference in the system performance, and generally we include these four partially illuminated gradients in the matrix calculation.

The late Walter Wild provided UnISIS with two basic control matrices: a least squares estimator and an optimal estimator (Wild et al. 1995; Wild 1997, 1998, and references therein). Wild created the matrices with his A+ software package. We have matrices for both a "small" central obscuration and a "large" central obscuration depending on whether or not the four central partially illuminated gradients are incorporated in the solution. All matrices are based on singular value decomposition under the assumption that the influence function of one actuator does not significantly affect the mirror surface at the positions of adjacent actuators. In truth, measurements made by Xinetics Inc. show an influence function at the 7 mm actuator spacing that induces a spillover motion $\sim 8\%$. For LGS operation only, the tip-tilt mode is projected out of the control matrix because a separate closed-loop tip-tilt system handles this atmospheric perturbation. For NGS operation, the tip-tilt correction remains in the control matrix. During NGS operation on the sky, we take care to guide the telescope so that the full stroke of the DM is not consumed by tip-tilt correction. On nights when the seeing in V band is better than $\sim 1.5''$, this is not a problem. On nights when the seeing is worse than this, we generally do not work.

6. CLOSED-LOOP CONTROL SYSTEM AND AO OPERATIONS

The original UnISIS closed-loop control system consisted of two quad C-40 digital signal processing (DSP) boards from EPICS mounted in a VME bus extension chassis and controlled by a 486 host computer. The matrix calculation was distributed among the eight DSP chips and was thereby done in parallel. The technology was already old when this first system was assembled in 1997. The aim at that time was to put the system

FIG. 4.—UnISIS control room. The large computer screen displays the active WFS signal. The tall rack in the background (closest to the door) holds the DM actuator HV control, and the shorter rack holds five small computers. Three run under Linux (one each for the two science cameras and one for the AO closed-loop control) and two run under Windows (one for the high-speed video image of the AO-corrected focal plane and one for the servo-controled motorized components.

together quickly in order to get UnISIS off to a fast start, but at its maximum operating rate, the DM actuators were updated by the old control system only 248 times per second. In mid-2004 the old control system was replaced by a significantly faster system designed and built to optimize speed. Both software system implementations—the old and the new—were done in collaboration with T. Schneider (RipTideRealTime Inc., Topanga Canyon, CA). We refer the reader to Schneider (2004) for a more detailed description of the new AO software design philosophy and especially its architecture. Schneider (2004) also contains a partial listing of code that determines the UnISIS Hartmann WFS gradients. We summarize in the following four paragraphs the basic overarching design characteristics of this real-time software, describe the system hardware, and then give its operational characteristics. The system speed and closed-loop control rates given here are the actual experimental values. They supersede preliminary estimates given by Schneider (2004). A photograph showing the main electronic components of the UnISIS control system are shown in Figure 4.

In the new UnISIS AO control system, both the graphical user interface and the AO matrix calculation for wavefront control—often called the reconstructor—are done in a single 2.4 GHz Pentium processor running RTLinux. Input data from the two E2V wavefront cameras (NGS and LGS) are delivered to the CPU on the main computer bus by two separate PCI interface cards from Astronomical Research Cameras, Inc. (ARC, San Diego, CA). Both E2V WFS cameras—located on the UnISIS optics table—communicate with the Pentium through high-speed fiber-optic data links.

The software consists of real-time and non-real-time components running in the processor kernel. I/O calls are issued to the non-real-time portion via a graphical interface. The matrix reconstructor calculation is given priority with occasional checks being made for interrupts (signaled by the user through the graphical interface). Little machine time is lost to these interrupts, so the AO closed-loop code runs extremely fast. Lessons learned from the first-generation UnISIS control system were applied to the second-generation system to optimize speed. The most significant of these involve the E2V camera data transfer timing and the block structure used for the PCI data transfer, which were optimized for the new AO control system by Robert Leach at ARC.

To insure low-noise WFS readout, each pixel in the E2V Hartmann array is given 2.52 μs in its respective CCD amplifier while being read, so a full set of 13×13 gradients (26×26 pixels) can be processed by the four CCD amplifiers in 426 μs, after which the fiber-optics link block-transfers the pixel values to the PCI card. The CCD camera electronics use an additional 59 μs for the CCD frame transfer and to skip unused pixels during the CCD readout. The total system overhead—after the WFS data arrive at the CPU until the DM actuator instructions are delivered—amounts to 121 μs. With a total system processing time of 606 μs and a WFS exposure time of 0.1 ms, UnISIS runs at a closed-loop speed of 1416 Hz. As the exposure time is lengthened—we do so in increments of 0.1 ms—the closed-loop speed is slowed accordingly.

Once the full set of DM actuator instructions is known from a single Hartmann WFS frame of data, this set of actuator values is transferred to a FIFO buffer that communicates with the Xinetics DM HV drive electronics rack. The FIFO buffer interface requires an additional 87 μs to accomplish its input/output function, and although this 87 μs contributes to the system latency, it does not alter the closed-loop speed because the FIFO transfer is done after the next WFS exposure has begun. The LGS closed-loop control system runs slightly faster than the NGS system because the LGS exposure time is set at a fixed 20 μs. The LGS light arrives in this short time period, and there is no need for the camera to integrate longer. On an experimental basis, we noticed a significant improvement in performance following the move from the original 248 Hz operation to the new and faster UnISIS computer control system.

7. ATMOSPHERIC DISPERSION CORRECTION SYSTEM

Light entering either of the two science cameras through a broadband filter would be dispersed by differential atmospheric refraction, and, if left uncorrected, AO images would be elongated in a direction perpendicular to the horizon. An ADC system was incorporated into UnISIS to avoid this problem. The ADC design follows the classical Risley prism concept where four prisms (two pairs of two prisms each) counter-rotate with respect to an axis perpendicular to the horizon. When the strong axis of the prism pairs are parallel and oppose each other, the dispersion correction strength is zero. As the prism pairs counter-rotate, the dispersion correction increases until they have each turned 180° and the prism strength reaches its maximum. At zenith no correction is required. The UnISIS prism pair reaches its maximum correction strength when the zenith angle of any target approaches 56° (air mass = 1.8). For a given observatory altitude (and a corresponding average atmospheric pressure), an optimal pair of glass types can be selected to best match the strength of the atmospheric refraction. For Mount Wilson the best glass types are LaNF21 and KF9 (Shelton & Baliunas 1994). The two LaNF21 prisms in UnISIS have wedge angles of 2.078° and center thicknesses of 8.8 mm, while the KF9 prisms have wedge angles of 3.125° and center thicknesses of 10.7 mm. Starlight traveling from the telescope's coudé focus toward the prism pair encounters the glass in the following order: LaNF21, KF9, KF9, LaNF21. Because the prism pairs must be free to rotate, the system was designed to have four air-glass surfaces and two glass-glass surfaces with index-matching oil where the glass meets. The four air-glass surfaces are coated with a broadband antireflection coating, but the two glass-glass surfaces were not. In its current state, the index-matching oil has not been applied.

To achieve true zero deviation for the central ray through the prisms, great care must be taken to match the axes of the two prisms as they are inserted into their mounts. If this condition is not met, then objects in the focal plane will "orbit" around the field center (at the final system focal plane) as the ADC is adjusted in strength. This means that the prisms, LaNF21+KF9, must be placed one on top of the other in the same mount with their wedge axes counter-aligned to a tolerance of 0.1° in rotational position. The same must be done for the second prism pair. The best way to achieve the alignment of each prism pair (before inserting each pair into its respective mount) is to transmit a test laser beam through the prism pair when the two prisms are nearly in contact. We placed very thin smooth shims between the LaNF21 and KF9 during the alignment procedure so the two prisms could be rotated during the adjustment process without scratching the optical surfaces where they meet. Reflections at each prism face will split the beam and create multiple images that orbit each other as the axes of the two prisms are rotated with respect to each other. It does not matter where the laser beam enters the prism pair (at the center of the optic or offset from the center) nor does it matter what the entrance angle is. During the alignment process (as the wedges are turned with respect to each other), the multiple images appear to orbit each other. When proper alignment is achieved and the relative wedge angle is zero, the multiple images fall along a straight line.

When the UnISIS ADC system was commissioned, it was helpful to have a color-sensitive video-rate CCD at the system focal plane. By pointing the telescope to bright stars at various zenith angles and at various azimuths and watching the focused image on the color CCD camera, it became relatively easy to determine the ADC's angular "strength" setting and the proper position angle of the prism pair based on the appearance of the star image in real-time color. When the ADC settings were close to correct, the star image became monochromatic. When these settings were incorrect, the color camera clearly showed dispersed spectral colors. The UnISIS ADC system runs under a servo-actuated positioning system. It automatically reads the telescope R.A. and decl., calculates the corresponding altitude and azimuth of the star, and uses these numbers to set the strength and position angle of the prism pair. The servo-control system evolved with time. The first ADC control system (built on a stand-alone PC) was too slow. In the second version, the PC was updated with a faster Linux operating system and an interface that accepts key information from the telescope and commands separate controllers that operate the rotating prism mounts.

8. TIP-TILT CLOSED-LOOP CONTROL SYSTEM

M7 in Figure 1 is a 100-mm diameter tip-tilt mirror built by Physik Instrumente (Auburn, MA). It is used only during LGS AO operation. During NGS AO operation M7 remains fixed, and the DM makes all wavefront corrections. Because a LGS carries no information on atmospheric tip-tilt, the tip-tilt signal comes from the NGS E2V CCD that sits behind M8 and senses its position from an on-axis star. Of course, this E2V camera serves the dual role of providing the WFS input during NGS operation and the tip-tilt input during LGS operation. To convert the NGS WFS into a tip-tilt camera, a mechanical lever is moved to swap the WFS lenslet array + camera optics with a simple lens that is used for LGS tip-tilt operation. The collimating optics are left in place because they are shared between the two optical systems. The simple lens can be easily changed, but at the present time the system is set up to provide an image scale of 0.14 arcsec pixel^{-1}. The UnISIS control system processes an area on the detector 26×26 pixels so the tip-tilt system views an area on the sky 3.74″ on a side.

9. THERMAL CONTROL ISSUES

On its way to the f/30 coudé focus, light from the telescope passes down a 250-mm diameter steel tube that is coaligned with the 2.5-m telescope's south polar axis. If a significant temperature difference exists between the coudé room and the observing chamber, air will flow either up or down this steel tube. The most common situation is for air to flow up the 250-mm diameter pipe as the evening air cools the observing chamber more quickly than it cools the coudé room. In some circumstances, this compromises both the astronomical image quality and the quality of the laser guide star beam. To eliminate this problem, an in-line exhaust fan was installed in a large horizontal air duct connecting the coudé room with an outside exhaust vent. With all doors to the coudé room closed, this fan can lower the pressure in the coudé room just enough to stop air from flowing up the 10-inch diameter steel tube. To achieve this balance, the in-line fan speed is adjusted with a variac as we monitor the 250-mm diameter steel tube for air flow. In this way the natural image quality is not compromised. This conclusion is based on a comparison of the uncorrected images we see at the 2.5-m coudé focus when compared to reports of nightly seeing from other facilities that operate on Mount Wilson.

10. UNISIS AO PERFORMANCE

To analyze the Strehl performance of UnISIS, we use the extended Marechal approximation (Marechal 1947), an approximation that works well with Strehl >0.2. If we designate the Strehl ratio with the symbol S and the total residual wavefront error with $K = \sigma^2_{\rm Tot}$, then following the relationship holds

$$\mathrm{S} \sim \mathrm{e}^{-K},$$

where the total wavefront variance (in radians^2) is the quadrature sum of all relevant contributors:

$$\sigma^2_{\rm Tot} = \sigma^2_{\rm Time} + \sigma^2_{\rm Fit} + \sigma^2_{\rm WFS} + \sigma^2_{\rm Speckle} + \sigma^2_{\rm Rem}.$$

Subscripts designate the following specific sources of wavefront error: temporal system lag (Time), DM fitting error (Fit), photon

TABLE 3
DETAILED NGS AO SYSTEM PERFORMANCE ANALYSIS

Date (UT)	Star	Exp	Data m_V	Filter	r_o	Strehl	$\sigma^2_{\rm Tot}$ (rad^2)	Marechal Prediction (rad^2) $\sigma^2_{\rm Times}$	$\sigma^2_{\rm Fit}$	$\sigma^2_{\rm Speckle}$	$\sigma^2_{\rm Rem}$
04 Aug 14	α Oph	3 s	2.08	z	16 cm	0.17	1.77	0.15	0.50	0.19	0.93
04 Aug 14	α Oph	1 s	2.08	H	34 cm	0.43	0.84	0.04	0.14	0.05	0.61
05 Jul 2	HIP85157	3 s	5.71	H	21 cm	0.60	0.51	0.15	0.31	0.12	0.0
05 Jul 2	HR7235	1 s	2.98	K_s	29 cm	0.67	0.40	0.09	0.19	0.07	0.05

counting errors in the wavefront sensor (WFS), WFS speckle noise (Speckle), and all remaining errors consolidated into the final remainder term (Rem). The analytic definitions for these errors are given in the Appendix. To calculate the σ^2 values, we rely primarily on Sandler (1999) but refer to Hardy (1998) to estimate the Greenwood frequency and Racine (2006) to calculate $\sigma_{\rm Speckle}$.

Table 3 can be used as a guide for understanding the performance of UnISIS. The left columns summarize the key empirical data (essentially the observed Strehl ratios) while the right columns list values (in rad^2) for individual terms in the Marechal approximation calculated for the conditions on each specific night at the observed wavelength. If there are no hidden problems in the operation of UnISIS, the observed Strehl ratio—i.e., $\sigma^2_{\rm Tot} = -\ln(\rm S)$—will match the sum of the σ^2 terms listed in the five left columns of Table 3. If the value in the final column is zero, then all contributions to the wavefront error are accounted for. One can see that the 2004 August 14 data show unexplained wavefront errors, but on 2005 July 2 all wavefront errors are understood. The data are discussed in turn from these two nights.

A comprehensive set of performance data was collected on 2004 August 14 (UT) before we began the upgrade to the new closed-loop control system in order to document the performance of the old system. Figure 5 shows two images from this observing run. We show them here for two reasons. First, they provide a way to assess the improvements provided by the new closed-loop system. Second, these images were incorporated into a comprehensive analysis of astronomical AO systems by Racine (2006) even though they have not been published before.

At Mount Wilson, 2004 August 14 (UT) was generally photometric. A few scattered clouds were present in the northern part of the sky, but they had no effect on the observations reported here because the bright target star α Ophiuchi used in these tests was located close to the meridian at an air mass 1.12. Upper atmospheric winds were slow, and we estimate the winds to have been 3 m s^{-1} based on online weather data available that night. The UnISIS closed-loop frame rate for NGS correction was 246 Hz.

A pair of images was collected simultaneously with the visible wavelength CCD camera behind an SDSS z-band filter (900 nm effective wavelength) and with the NIRIM detector array behind a standard H-band filter (1.65 μm effective wavelength). We estimate the seeing at FWHM $\sim 1.0''$ (based on the FWHM of uncorrected images at 550 nm we observed that night). If we convert this seeing into effective r_o values using

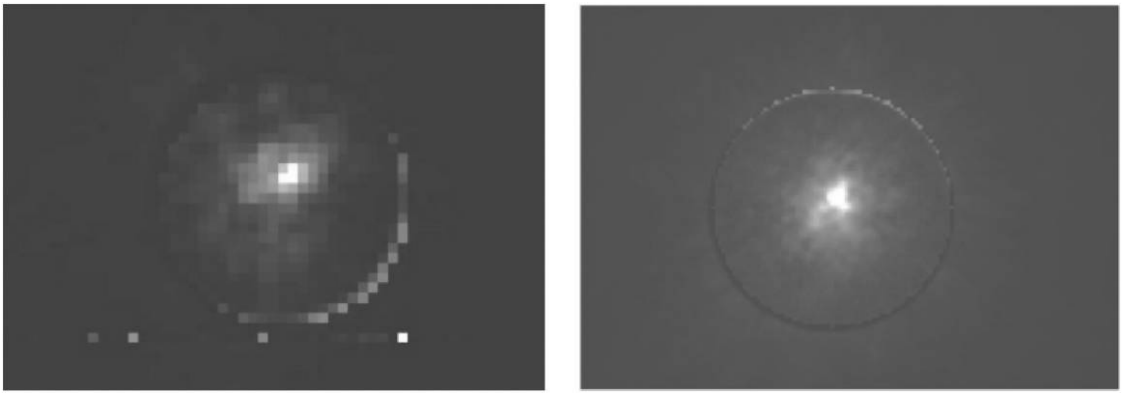

FIG. 5.—NGS images of α Oph. taken on 2004 August 14 (UT) *Left*: 1 s H-band image taken with NIRIM yielding Strehl ~0.43. *Right*: 3 s z-band image taken with the 2KCCD yielding Strehl ~0.17. A circular discontinuity of diameter 2.11″ can be seen where the reflectivity changes on the M8 pinhole mirror from bare glass (inside) to aluminum (outside), and this sets the scale of the images. North is at the bottom and east to the left. In both images the intensities inside the pinhole were rescaled to make the transition look continuous. The residual ring comes from that adjustment process. Both images are displayed with a logrithmic stretch in intensity to show with equivalent weight the highest and lowest intensity levels. Note that the H-band image was captured with pixels 0.08″ on a side and is therefore slightly undersampled. See the electronic edition of the *PASP* for a color version of this figure.

TABLE 4
NGS STREHL'S 2005 JULY 2 (UT)

Obs.	Star	Filter	m_V	Exposure	Air Mass	Strehl
1	14 Her	H	6.67	3 s	1.02	0.70
2	14 Her	H	6.67	3 s	1.03	0.50
3	HIP 85157	H	5.71	3 s	1.03	0.55
4	HIP 85157	H	5.71	3 s	1.03	0.80
5	HIP 85157	H	5.71	3 s	1.03	0.30
6	HR 7235	H	2.98	1 s	1.07	0.45
7	HR 7235	H	2.98	1 s	1.07	0.45
8	HR 7235	K_s	2.98	1 s	1.10	0.60
9	HR 7235	K_s	2.98	1 s	1.10	0.45
10	HR 7235	K_s	2.98	1 s	1.10	0.85
11	HR 7235	K_s	2.98	1 s	1.10	0.50
12	HR 7235	K_s	2.98	1 s	1.10	0.55
13	HR 7235	K_s	2.98	3 s	1.10	0.40

the formalism described by Racine (2006) that incorporates a value for the outer scale (we assume $L = 15$ m), we find $r_o = 16$ cm (at 900 nm z-band) and 34 cm (at 1.65 μm H band). Because we do not know the exact value of L for this night (nor for 2005 July 2 discussed below), we adopt for both nights the reasonable estimate of $L = 15$ m based on turbulence measurements of Linfield et al. (2001) made at Mount Palomar, the closest observatory to Mount Wilson where any value of L has been measured. r_o is not strongly dependent on the precise value we adopt for L.

While the NGS images from 2004 August 14 show reasonable Strehl ratios, Table 3 indicates that there were hidden problems in UnISIS at that time. The most reasonable explanation is related to slaving the innermost and outermost actuators on the deformable mirror. At the time of this observing run, these actuators were "floating" in the sense that the AO control system was sending them no information. Notice that $\sigma_{\rm Rem}$ shows a larger value for the z-band image than for the H-band image. This is a natural outcome for a fixed physical deformation of the DM because the units (rad^2) are wavelength dependent, and a fixed physical deformation will appear to have a larger effect at shorter wavelengths.

A second set of NGS Strehl performance data was taken on the night of 2005 July 2 (UT). The new AO closed-loop computer control system had just been installed, and we had just implemented the DM actuator slaving scheme described in § 5. The weather was photometric, but the uncorrected image quality was mediocre (FWHM $\sim 1.35''$ at 550 nm based on our visual estimates of the image quality). Some image degradation was caused by a layer of high altitude wind that we estimate had a speed of 10 m s^{-1}. Most of the image degradation appears to have come from lower altitudes where the wind speed was smaller.

Table 4 shows a summary of 13 PSF observations we made on 2005 July 2 where we list observations in both the H band and the K_s band. We provide in Table 4 an estimate of the Strehl ratio for each image. This estimate is based on the ratio of two flux measurements: a Gaussian fit to the diffraction-limited image core; and the integrated total stellar flux in a box $2''$ on a side. These Strehl estimates are accurate to ± 0.05 and are not corrected for image saturation effects (see below). From this list of 13 images, we present detailed information for one H band

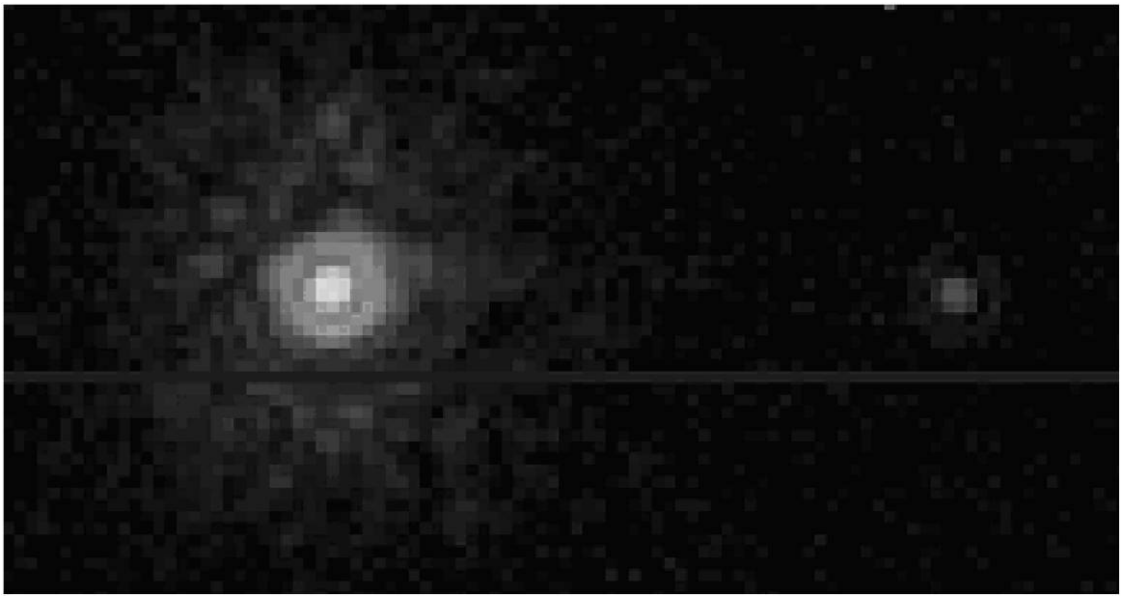

FIG. 6.—NGS K_s-band image taken on 2005 July 5 (UT) of HR 7237 ($m_V = 2.98$) at air mass 1.10. The exposure time is 1 s. After correcting for saturated pixels in the main image (based on the image profile of the ghost image seen to the right), we find a Strehl ~0.67. The first diffraction ring is clearly resolved. Individual pixels are $0.08''$ on a side, and the ghost image is located $4.3''$ from the primary image, and this sets the scale of the image. North is at the bottom and east the left. This image is displayed with a logrithmic stretch in intensity to show both the highest and lowest intensity levels.

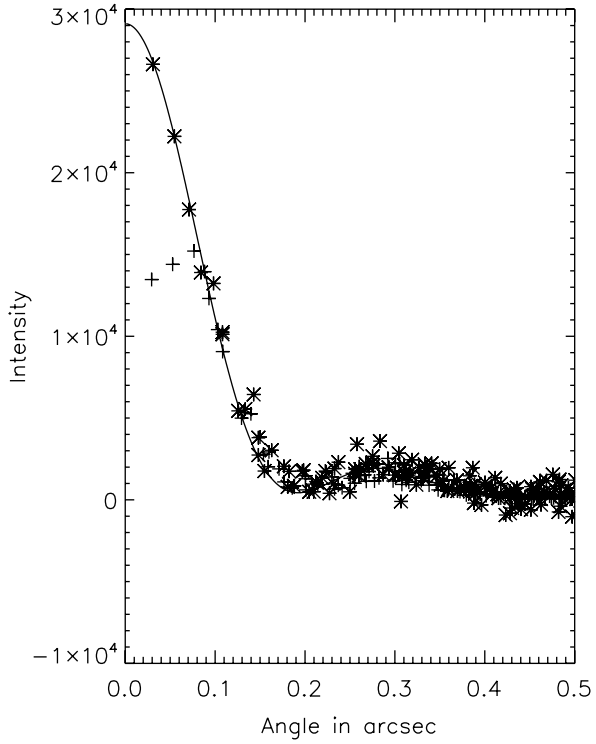

FIG. 7.—Data from two radial intensity profiles of the K_s-band image from Fig. 6 are shown here. Plus signs come from the main image and asterisks from the ghost image. The intensities of the ghost image have been multiplied by 100 to match those from the central image. The smooth line is the sum of the telescope diffraction pattern (67% of the total flux) and a Gaussian (33% of the total flux). The Gaussian has FWHM $= 1.05''$ (seeing width at 2.12 μm), and the diffraction pattern represents a 2.5-m aperture with a central obscuration of diameter 0.82 m. Three central plus symbols fall well below the theoretical curve because the main image is saturated in the core.

(number 3) and one K_s band image (number 8). In both cases we chose representative examples and not the images with the best estimated Strehl. This was done to avoid lucky observer effects that might be associated with short exposure images.

Figure 6 shows the selected K_s-band image, a 1 s exposure taken at air mass 1.10 of the star HR7237 ($m_V = 2.98$). Despite the poor seeing, UnISIS delivered a Strehl ratio of 0.67. The central pixels of the main image are saturated, but they are not in a ghost image (formed by internal reflections inside the ADC) that can be seen off to the right in Figure 6. By scaling the primary and ghost images appropriately, we produced the radial intensity profile for the K_s-band image that we show in Figure 7. The continuous line in the plot shows a theoretical fit to the image profile as described in the legend for Figure 7. We note that the central diffraction-limited core sits on top of uncorrected light that remains in a halo with FWHM that of the natural seeing. Our fit to the width of this uncorrected light confirms the visual seeing estimate we give above.

Figure 8 shows the selected H-band image, a 3 s exposure taken at air mass 1.05 of the star HIP 85157 ($m_V = 5.71$). UnISIS delivered a Strehl ratio of 0.60. Because we were using pixels $0.08''$ on a side and the diffraction-limited image core has a FWHM $\sim 0.14''$, this image was slightly undersampled by the camera so the first diffraction ring is not as distinct as that shown in Figure 6. Again, the central pixels of the main image are saturated, but those of the secondary image are not. Our Strehl calculation was done after correcting the central pixels of the main image for saturation effects as described above.

11. CURRENT STATUS

UnISIS is a fully developed and operational AO system that will continue to be used for both science observations and for tests of both AO and laser guide star projection techniques. It can reach Strehl performance of 0.67 at K_s band when the natural images are $1.35''$ FWHM at 550 nm. We anticipate even higher Strehl ratios during the best seeing conditions at Mount Wilson Observatory.

We plan to make further innovative technical contributions using UnISIS. It is a perfect system for tests of this kind especially because of the excellent telescope optics and the high density of actuators in the telescope pupil (20 cm separation). For example, in Chakraborty et al. (2005) we tested a complex coronagraphic configuration that included both a Gaussian-shaped pupil mask as well as a small focal plane mask while UnISIS worked (on the bench) with an AO-corrected wavefront at $\sim 1/30$ wave at 830 nm. UnISIS provides the means to conduct LGS tests, and our future work will involve tests of extreme adaptive optics, ground-layer AO correction methods, and laser beam shaping to further increase the return signal from the UnISIS excimer laser.

Three awards from the National Science Foundation (Astronomy Advanced Technology and Instrumentation) were used to construct UnISIS: AST-8918878 to purchase the Excimer laser system and conduct feasibility tests of Rayleigh scattered laser guide stars, AST-9220540 for the main UnISIS instrument development phase, and AST-0096741 for the UnISIS science commissioning phase. We acknowledge additional support from the University of Illinois Astronomy Department and the University of Illinois College of Liberal Arts and Sciences. We thank two directors of Mount. Wilson Institute (the late Robert Jastrow and current director Hal McAlister) for hosting the UnISIS project at the 2.5-m telescope on Mount Wilson. Innumerable people assisted us while UnISIS was under development, and we thank them all for their efforts: E. Harvey Richardson, Tom Schneider, Margaret Meixner, Peter McCullough, Tao Wang, Sam Crawford, Jie Zou, Daniel Goscha, Dan Bullock, Ray DuVarney, Robert Cadman, Victor Castillo, Sean Hoss, Larry Webster, Kirk Palmer, Joe Russell, Bill Knight, Mike Bradford, Jim Strogen, Darrel Moon, and Alex Bogdanovich. We also thank the referee for suggestions that improved our presentation.

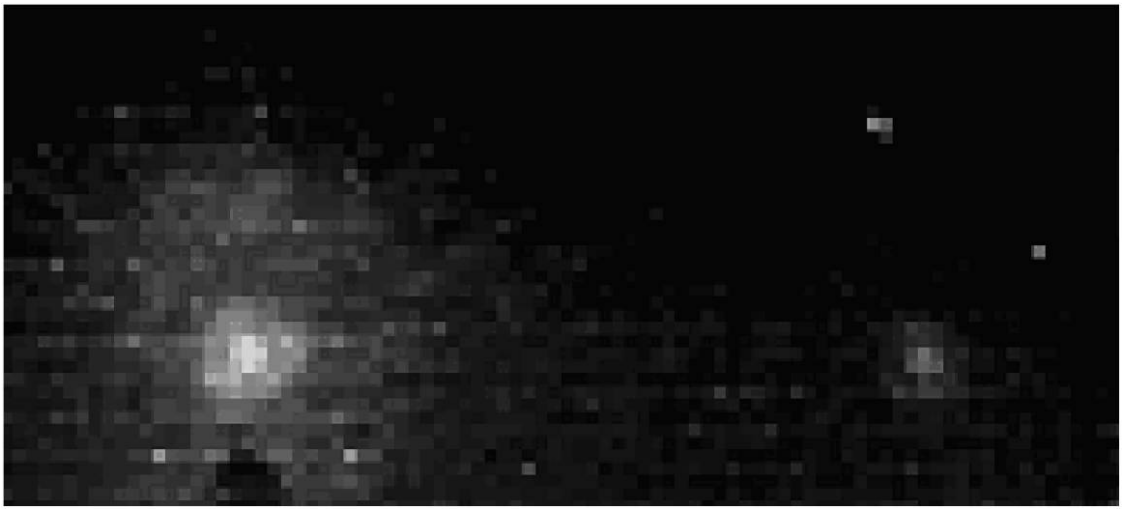

FIG. 8.—NGS H-band image taken on 2005 July 2 (UT) of HIP 85157 ($m_V = 5.71$) at air mass 1.05. The exposure time is 3 s. After correcting for saturated pixels in the main image (based on the image profile of the ghost image seen to the right), we find a Strehl ~0.60. As in Fig. 6, the separation between the main image and the secondary image is 4.3″ and this sets the scale of the image. North is at the bottom and east the left. Because individual pixels are 0.08″ on a side, the diffraction-limited core is undersampled. The dark region just below the main image is a latent image from a previous exposure. Our Strehl calculation excluded this region from the analysis. This image is displayed with a logrithmic stretch in intensity to show both the highest and lowest intensity levels.

APPENDIX A

MARECHAL TERMS

It is conventional when calculating wavefront errors with the extended Marechal approximation to use units of rad^2 for each σ, and we follow this convention here. To convert wavefront errors into physical units like nanometers, note that values in rad^2 are quoted for a specific wavelength λ, and they can be converted to nanometers with the relationship 1 radian $= \lambda/2\pi$.

$\sigma_{\rm Time}$: Temporal system lag (see § 12.3.4 in Sandler 1999 for the basic definition and § 9.4.3 in Hardy 1998 for a discussion on estimating the Greenwood frequency)

$$\sigma^2_{\rm Time} = ({\rm f_G}/{\rm f_s})^{5/3}\ {\rm rad}^2,$$

where $\rm f_G$ is the Greenwood frequency and $\rm f_s$ is the system frequency. In the special case of a single turbulent layer moving at wind velocity v in an atmosphere characterized by the coherence length r_o at the wavelength of the observations, $\rm f_G = 0.427\ v/r_o$. The system frequency in these calculations is assumed to be $1/10$ the closed-loop update rate. This update rate was 248 Hz on 2004 August 14 and 623 Hz on 2005 July 2.

$\sigma_{\rm Fit}$: Wavefront fitting error (see § 12.3.4 in Sandler 1999 for a basic definition)

$$\sigma^2_{\rm Fit} = 0.35(20\ {\rm cm}/r_o)^{5/3}\,{\rm rad}^2,$$

where the coefficient is taken to be 0.35 rather than the generally adopted value of 0.3 because we incorporate in this term both the conventional wavefront fitting error (at 0.3) as well as what is often called the reconstructor error. The latter scales in the same manner as the conventional wavefront fitting error with an additional coefficient of 0.05. The 20 cm in the numerator of our expression represents the separation between DM actuators as seen in the telescope pupil, and to get the appropriate value for this error, r_o must adopted for the wavelength of the observation.

$\sigma_{\rm WFS}$: A column for this term is not included in Table 4 because all values are essentially zero as explained below (see § 11.1.2.1 in Sandler 1999)

$$\sigma^2_{\rm WFS} = 1.4\pi^2/{\rm N_{photons}rad}^2 = 13.8/{\rm N_{photons}rad}^2.$$

All NGS tests of UnISIS reported here were made on bright target stars, so $\rm N_{photons} > 2000$ per subaperture. The wavefront sensor error is essentially zero in these circumstances.

$\sigma_{\rm Speckle}$: Wavefront speckle error (see Racine 2006)

$$\sigma^2_{\rm Speckle} = 0.134(20\ {\rm cm}/r_o)^{5/3}(700\ {\rm nm}/\lambda_{\rm obs})^2,$$

where we have inserted into this equation 20 cm as the projected subaperture diameter at the telescope pupil and 700 nm as the peak wavelength of the NGS WFS.

$\sigma_{\rm Rem}$: Remaining wavefront error left to be explained by unknown sources. We suspect that the biggest contributor on 2004 August 14 to $\sigma_{\rm Rem}$ came from DM actuators that were left floating around the outer perimeter of the pupil. By the time the 2005 July 2 observations were made, these actuators were slaved to their nearest radial neighbors, and this term was significantly reduced.

REFERENCES

Babcock, H. W. 1953, PASP, 65, 229
Baranec, C., et al. 2009, ApJ, 693, 1814
Boccas, M., et al. 2006, Proc. SPIE, 6272, 114
Chakraborty, A., Thompson, L. A., & Rogosky, M. 2005, Opt. Express, 13, 2394
Chun, M., et al. 2008, Proc. SPIE, 7015 (in press)
Foy, R., & Labeyrie, A. 1985, A&A, 152, L29
Fugate, R. Q., et al. 1994, J. Opt. Soc. Am. A, 11, 310
Gardner, C. S., Welsh, B. M., & Thompson, L. A. 1990, Proc. IEEE, 78, 1721
Happer, W., MacDonald, G. J., Max, C. E., & Dyson, F. J. 1994, J. Opt. Soc. Am. A, 11, 263
Hardy, J. W. 1998, Adaptive Optics for Astronomical Telescopes (Oxford: Oxford Univ. Press)
Linfield, R. P., et al. 2001, ApJ, 554, 505
Marechal, A. 1947, Rev. d'Optique, 26, 257
Meixner, M. M., et al. 1999, PASP, 111, 997
Milton, N. M., et al. 2008, Proc. SPIE, 7015, in press
Racine, R. 2006, PASP, 118, 1066
Rigaut, F., Ellerbroek, B., & Flicker, R. 2000, Proc. SPIE, 4007, 1022
Ritchey, G. W. 1928, J. RAS Canada, 22, 359
Roberts, J, et al. 2008, Proc. SPIE, 7015, in press
Roberts, L. C., Jr., & Neyman, C. R. 2002, PASP, 114, 1260
Rutten, R. G. M., & Talbot, G. 2005, ING Newsletter, 10, 11
Sandler, D. G. 1999, in Astronomical Adaptive Optics, ed. Roddier, F. (Cambridge: Cambridge Univ. Press)
Schneider, T. G. 2004, Dr. Dobb's Journal, 29, 24
Shelton, C., & Baliunas, S. 1994, in Optical Astronomy from the Earth and Moon, ed. Pyper, D. M., & Angione, R. J. (San Fancisco: ASP)
Shelton, C., et al. 1997, Proc. SPIE, 3126, 321
Strobele, S., et al. 2006, Proc. SPIE, 6272, 9
Takami, H., et al. 2004, PASJ, 56, 225
Teare, S. W., & Thompson, L. A. 2002, PASP, 114, 125
Teare, S. W., et al. 2000, PASP, 112, 1496
Thompson, L. A., & Castle, R. M. 1992, Opt. Lett., 17, 1485
Thompson, L. A., Castle, R. M., & Carroll, D. L. 1991, Proc. SPIE, 1542, 110
Thompson, L. A., & Gardner, C. S. 1987, Nature, 328, 229
———. 1989, Proc. SPIE, 1114, 184
Thompson, L. A., & Teare, S. W. 2002, PASP, 114, 1029 (Paper I)
Thompson, L. A., et al. 2003a, Proc. SPIE, 4839, 44
———. 2002, PASP, 114, 1143
———. 2003b, Proc. SPIE, 5169, 11
———. 2004, Proc. SPIE, 5490, 90
Tokovinin, A., et al. 2004, Proc. SPIE, 5490, 870
Toomey, D. W., & Ftaclas, C. 2003, Proc. SPIE, 4841, 889
Wild, W. J. 1997, Proc. SPIE, 3126, 278
———. 1998, Proc. SPIE, 3353, 1164
Wild, W. J., et al. 1995, Proc. SPIE, 2534, 194
Wizinowich, P. L., et al. 2006, PASP, 118, 297